Extra stress-mediated acoustic streaming in a surface acoustic wave driven microchannel filled with second-order fluids

Pradipta Kr. Das and Venkat R. Bhethanabotla*
Department of Chemical, Biological, and Materials Engineering, University of South Florida, Tampa, Florida 33620-5350, USA

(Received 20 March 2022; accepted 18 July 2022; published 29 July 2022)

This study investigates the acoustic streaming phenomena in a standing surface acoustic wave driven microfluidic channel filled with second-order fluids. We have developed a multiple-timescale-based theoretical model where a perturbation technique was adopted to separate the fast and slow timescales associated with the oscillatory flow field (i.e., acoustic field) and the mean flow field (acoustic streaming), respectively. The governing equations have been expressed in nondimensional form to effectively show the dependence of the acoustic streaming fields on Reynolds number (Re), Deborah number (De), and the ratio of material constants related to normal stress coefficients (b). Contrary to our intuition, we observed that with increasing Deborah number (which is a measure of the extra stress present in the second-order fluids), acoustic streaming first increases and thereafter, a further increase in Deborah number leads to a gradual suppression of streaming. Our study also reveals that the acoustic field and the acoustic radiation force show negligible dependence on the fluid rheology. For the following ranges, $0.08 \leqslant \mathrm{Re} \leqslant 0.32$, $0 \leqslant \mathrm{De} \leqslant 1$, and $0 \leqslant b \leqslant 100$, the maximum variation of the acoustic streaming is observed to be $\sim$161.3%, whereas the variation in the acoustic field stays within just 0.15%. This significant finding can help design efficient acoustofluidic systems that can manipulate acoustic streaming without affecting the acoustic radiation forces, as strong acoustic streaming can impair the acoustofluidic devices.

DOI: 10.1103/PhysRevFluids.7.074404

I. INTRODUCTION

The use of ultrasound in fluids has garnered significant attention over the past few decades due to its various applications in biomedical and nanotechnology-based fields. The interaction of acoustic wave and fluid causes a fast oscillatory fluid motion (called acoustic field) and in addition to that, a steady flow (called acoustic streaming) is slowly evolved over time. The discovery of this acoustic streaming traces back to the early 19th century when Ørsted (1809) and Savart (1827) observed different granular motions of fine and coarse powders over a vibrating Chladni plate. Later, Faraday [1], in his Chladni plates experiments, demonstrated acoustic streaming caused by air. The preliminary understanding of acoustic streaming was extended further when Dvorák (1876) noticed acoustic streaming in a Kundt tube actuated via a standing sound wave. Following these works, several theoretical and experimental studies were performed to broaden the understanding and the applicability of the acoustic streaming phenomena. The steady flow adjacent to any oscillating solid boundary is termed Schlichting streaming [2], and above that, a counter-rotating flow (called Rayleigh streaming [3]) is generated. Other than the viscous boundary layer, acoustic streaming can also be developed in the fluid bulk and it is known as Eckart streaming [4]. It is already

*bhethana@usf.edu

established that in Rayleigh streaming, there is an effective slip velocity observed at the interface of the boundary layer and the fluid bulk. Nyborg [5] was the first to provide an analytical expression for the slip velocity near an arbitrary smooth surface, which was later modified by Lee and Wang [6]. Researchers [7,8] have also provided analytical solutions for the acoustic streaming for simple geometries such as flow-through channels and flow-past cylinders. In his publication in 1978, Lighthill [9] pointed out that the Reynolds stress divergence, which results from the attenuation of acoustic energy flux, indeed acts as a driving force for acoustic streaming. Acoustic streaming can be used for microscale mixing [10–15], enhancement of heat transfer [16–18], and electrodeposition [19], etc. It is notable here that pressure acoustic theory is a widely used theory for acoustofluidics, although, it neglects the viscous boundary layer. Recently, Bach and Bruus [20] modified that and provided a pressure acoustic theory for curved elastic cavities where the viscous boundary layer was considered explicitly.

The particles or cells suspended in the fluid experience a mean force, called acoustic radiation force, due to the reflection of the sound wave from the particle surface. This acoustic radiation force [21,22] is utilized as a noninvasive tool to manipulate [23–26], remove [15,27–29], trap [30–34], lyse [35,36], concentrate, or sort [27,37–41] cells and particles [42,43]. It is established that this acoustic radiation force is proportional to the square of the particle size [44–46], and there exists a critical size above which the particle motion is dominated by the acoustic radiation force. Below that particle size, streaming drag force dominates over acoustic radiation force, and the motion of the particle is maneuvered by only the viscous drag. Nam *et al.* [47] successfully demonstrated that platelets can be separated from whole blood by utilizing the acoustic radiation force generated via a standing surface acoustic wave (SAW)-driven microfluidic system. Separation of circulating tumor cells (CTCs) from clinical samples was also possible by using a tilted angle SAW [40] or a vertical acoustic resonator [48]. Baasch *et al.* [49] demonstrated that for heavy particles, the acoustic radiation force can be significantly influenced by the acoustic microstreaming. Bjerknes force is also proven to be an effective means to manipulate the autonomous motions of micromotors [26,34,50,51]. Based on the broad applicability of acoustic streaming and acoustic radiation force in biomedical and small-scale activities, there is a need for controlling the streaming or the acoustic radiation forces. For instance, Hoyos and Castro [52] experimentally showed that acoustic streaming can be suppressed by using a pulsed actuation. However, the mechanism for the suppression is not yet understood [53]. This is often required since a strong acoustic radiation force causes significantly higher acoustic streaming which can impair the acoustic devices. Recently, Bach and Bruus [54] proposed shape-optimized channels for acoustic streaming suppression while the acoustic radiation forces remain unaltered.

Even though a large amount of literature is available on acoustic streaming, most studies are limited to Newtonian fluids. However, it is observed from a few studies that non-Newtonian fluid rheology can significantly affect acoustic streaming. Frater [55] analyzed acoustic streaming of an electroviscous fluid near a cylindrical particle and showed how elasticity modulates the streaming fields. Powell [56] studied the propagation of a finite amplitude planar acoustic wave in a viscoelastic fluid and reported a streaming reversal in the extreme viscoelastic regime. Doinikov *et al.* developed an analytical model to study the acoustic streaming [57] and the acoustic radiation force [58] of a solid particle in Oldroyd-B fluids. Das *et al.* [59] presented an analytic model to characterize the inner streaming in second-order fluids near a boundary. Their work showed the influence of extra stress and fluid compressibility on inner streaming.

In this contribution, we studied numerically the acoustic streaming and the acoustophoretic motion of particles for a bottom-actuated microchannel filled with second-order fluids. Perturbation technique was applied to the governing Navier-Stokes equation to separate the inherent fast and slow timescales, and the resulting net flow fields were expressed in time-averaged form to obtain the acoustic streaming. We demonstrate that acoustic streaming can be suppressed by altering the fluid rheology. It is observed that the extra stress present in the second-order fluids has a negligible impact in modulating the acoustic pressure; however, it can reduce the acoustic streaming drastically.

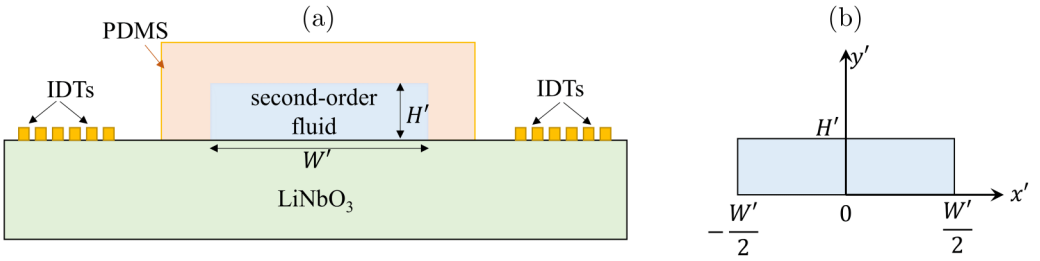

FIG. 1. (a) Schematic illustration of the physical problem depicting the standing surface acoustic wave driven microfluidic channel filled with second-order fluid. The microchannel is made of polydimethylsiloxane (PDMS) and is placed on lithium niobate substrate. IDTs are etched on the lithium niobate substrate, and the excitations of the IDTs generates surface acoustic waves. (b) Schematic of the corresponding computation domain consisting of the fluid only, with appropriate coordinate system.

II. MATHEMATICAL FORMULATION

A. Governing equations and boundary conditions

We consider a PDMS (polydimethylsiloxane) microchannel of width W' and height H', placed on a lithium niobate piezoelectric substrate as shown in Fig. 1. The PDMS microchannel contains a compressible second-order fluid having static density ρ_0 and dynamic viscosity η. Under the influence of acoustic excitation, the fluid density changes and can be denoted as ρ'. The sonic speed in the fluid is denoted as c_0. The governing equations for the fluid flow are given by

$$\frac{\partial \rho'}{\partial t'} + \nabla' \cdot (\rho' \mathbf{v}') = 0, \tag{1a}$$

$$\rho' \left[\frac{\partial \mathbf{v}'}{\partial t'} + (\mathbf{v}' \cdot \nabla')\mathbf{v}' \right] = -\nabla' p' + \nabla' \cdot \tau'. \tag{1b}$$

In the above, p', $\mathbf{v}' = u'\mathbf{e}_{x'} + v'\mathbf{e}_{y'}$, are the pressure and velocity of the fluid, respectively. $\mathbf{e}_{x'}$ and $\mathbf{e}_{x'}$ are the unit vectors along x' and y', respectively; t' is the time. The shear stress is given by $\tau' = 2\eta\mathbf{A}' + \alpha_1[\frac{\partial \mathbf{A}'}{\partial t'} + (\mathbf{v}' \cdot \nabla')\mathbf{A}' + \mathbf{A}' \cdot (\nabla'\mathbf{v}') + (\nabla'\mathbf{v}')^T \cdot \mathbf{A}'] + \alpha_2 \mathbf{A}'^2$, where α_1, α_2 are material constants related to normal stress coefficients and $\mathbf{A}'$ is the rate of strain tensor in the fluid given by $\mathbf{A}' = (1/2)(\nabla'\mathbf{v}' + \nabla'\mathbf{v}'^T)$. For acoustic oscillations with small amplitude, a linear constitutive relationship correlating density, ρ' with pressure, p' can be assumed, and it is expressed as [60–62] $p' = \rho' c_0^2$. The fluid inside the PDMS microchannel is actuated via a standing surface acoustic wave (SSAW) generated via ac excitations of the interdigital transducers on lithium niobate piezoelectric substrate, and the x' and y' components of the SSAW displacement field are given by [61,62]

$$d'_{x'} = \xi u'_0 (e^{-c'_d(W'/2 - x')} e^{ik'_x(x' - W'/2)} + e^{-c'_d(x' + W'/2)} e^{-ik'_x(x' - W'/2)}) e^{i\omega t'}, \tag{2a}$$

$$d'_{y'} = u'_0 (e^{-c'_d(W'/2 - x')} e^{i\{k'_x(x' - W'/2) + \pi/2\}} + e^{-c'_d(x' + W'/2)} e^{-i\{k'_x(x' - W'/2) + \pi/2\}}) e^{i\omega t'}, \tag{2b}$$

where ω and $k_{x'}$ are the angular frequency and the wave vector of the SSAW. u'_0 is the SAW displacement amplitude along the y' direction, and ξ is the ratio of the displacement amplitudes in x' and y' directions. The attenuation coefficient of the SAW is given by $c'_d = \rho_0 c_0 / \rho_{LN} c_{LN} \lambda$, where ρ_{LN} and c_{LN} are the density and the speed of SAW in lithium niobate along the x' direction, respectively; λ is the wavelength of the SSAW on the piezoelectric surface. For the side and top walls, the PDMS allows us to use the acoustic impedance boundary condition prescribed by

$$p' = Z'_w \mathbf{n} \cdot \mathbf{v}'. \tag{3}$$

In the above, Z'_w is the acoustic impedance of the PDMS wall and is given by $Z'_w = \rho_w c_w$, where c_w and ρ_w are sonic speed and density of PDMS, respectively.

B. Nondimensionalization of the governing equations and the boundary conditions

The governing equations and the associated boundary conditions are rendered dimensionless using the following dimensionless variables: $x = \frac{x'}{k^{-1}}$, $y = \frac{y'}{k^{-1}}$, $\rho = \frac{\rho'}{\rho_0}$, $\mathbf{v} = \frac{\mathbf{v}'}{c_0}$, $p = \frac{p'}{\rho_0 c_0^2}$, and $t = \frac{t'}{\omega^{-1}}$, where k is the acoustic wave vector inside the fluid and is given by $k = \omega/c_0$. The nondimensionalized governing equations are therefore written as

$$\frac{\partial \rho}{\partial t} + \nabla \cdot (\rho \mathbf{v}) = 0, \tag{4a}$$

$$\rho\left[\frac{\partial \mathbf{v}}{\partial t} + (\mathbf{v} \cdot \nabla)\mathbf{v}\right] = -\nabla p + \frac{\varepsilon}{\mathrm{Re}} \nabla \cdot \tau, \tag{4b}$$

where $\mathrm{Re} = \frac{\rho_0 k^{-1}(u'_0 \omega)}{\eta}$ is the Reynolds number, and the acoustic Mach number of the system is given by $\varepsilon = u'_0/k^{-1}$. Please note here that the Reynolds number has been defined by considering the reference velocity as $u'_0\omega$, which is nothing but the velocity amplitude of the SSAW. Dimensionless shear stress, $\boldsymbol{\tau}$, is expressed in terms of Deborah number De as

$$\boldsymbol{\tau} = \begin{pmatrix} 2\frac{\partial u}{\partial x} & \frac{\partial u}{\partial y} + \frac{\partial v}{\partial x} \\ \frac{\partial u}{\partial y} + \frac{\partial v}{\partial x} & 2\frac{\partial v}{\partial y} \end{pmatrix} + \mathrm{De}\begin{pmatrix} s_{xx} & s_{xy} \\ s_{yx} & s_{yy} \end{pmatrix}, \tag{5}$$

where $\mathrm{De} = \frac{\alpha_1 c_0}{\eta k^{-1}}$, and $\mathbf{v} = u\mathbf{e}_x + v\mathbf{e}_y$. The first term on the right-hand side denotes Newtonian stress, whereas the second term indicates the extra stress present in the second-order fluid, and its different components are given by

$$\begin{aligned}
s_{xx} &= \frac{\partial^2 u}{\partial t \partial x} + u\frac{\partial^2 u}{\partial x^2} + v\frac{\partial^2 u}{\partial x \partial y} + (2+b)\left(\frac{\partial u}{\partial x}\right)^2 + \left(1+\frac{b}{4}\right)\left(\frac{\partial v}{\partial x}\right)^2 \\
&\quad + \left(1+\frac{b}{2}\right)\frac{\partial u}{\partial y}\frac{\partial v}{\partial x} + \frac{b}{4}\left(\frac{\partial u}{\partial y}\right)^2; \\
s_{xy} = s_{yx} &= \frac{1}{2}\left(\frac{\partial^2 u}{\partial t \partial y} + \frac{\partial^2 v}{\partial t \partial x} + u\frac{\partial^2 u}{\partial x \partial y} + u\frac{\partial^2 v}{\partial x^2} + v\frac{\partial^2 u}{\partial y^2} + v\frac{\partial^2 v}{\partial x \partial y}\right) + \left(\frac{3+b}{2}\right)\frac{\partial u}{\partial x}\frac{\partial u}{\partial y} \\
&\quad + \left(\frac{3+b}{2}\right)\frac{\partial v}{\partial x}\frac{\partial v}{\partial y} + \left(\frac{1+b}{2}\right)\frac{\partial u}{\partial x}\frac{\partial v}{\partial x} + \left(\frac{1+b}{2}\right)\frac{\partial v}{\partial y}\frac{\partial u}{\partial y}; \\
s_{yy} &= \frac{\partial^2 v}{\partial t \partial y} + u\frac{\partial^2 v}{\partial x \partial y} + v\frac{\partial^2 v}{\partial y^2} + \frac{b}{4}\left(\frac{\partial v}{\partial x}\right)^2 + \left(1+\frac{b}{4}\right)\left(\frac{\partial u}{\partial y}\right)^2 \\
&\quad + \left(1+\frac{b}{2}\right)\frac{\partial u}{\partial y}\frac{\partial v}{\partial x} + (2+b)\left(\frac{\partial v}{\partial y}\right)^2.
\end{aligned} \tag{6}$$

The nondimensionalized boundary conditions are prescribed here. At the fluid bottom, the displacement boundary conditions are

$$d_x = \xi\varepsilon(e^{-c_d(W/2-x)}e^{ik_x(x-W/2)} + e^{-c_d(x+W/2)}e^{-ik_x(x-W/2)})e^{it}, \tag{7a}$$

$$d_y = \varepsilon(e^{-c_d(W/2-x)}e^{i\{k_x(x-W/2)+\pi/2\}} + e^{-c_d(x+W/2)}e^{-i\{k_x(x-W/2)+\pi/2\}})e^{it}. \tag{7b}$$

Here $d_x = d'_{x'}/k^{-1}$, $d_y = d'_{y'}/k^{-1}$, $c_d = c'_d k^{-1}$, $W = W'/k^{-1}$, and $k_x = k_{x'}k^{-1}$. At the side and top walls,

$$p = Z_w \mathbf{n} \cdot \mathbf{v}, \tag{8}$$

where the nondimensionalized acoustic impedance of the PDMS is expressed as $Z_w = \frac{Z'_w}{\rho_0 c_0}$.

C. Separation of timescales

The present theoretical study faces significant challenges due to the inherent multiple timescales involved in the problem. The fast-oscillating SSAW generates a fast-oscillating flow field (i.e., associated with fast timescale), and the nonlinearity in the flow dynamics adds a slowly moving fluid motion (i.e., associated with slow timescale). To tackle the issue, we employed a perturbation method to separate the fluid response corresponding to (i) a hydrostatic part which defines the unperturbed flow field before acoustic excitation, (ii) an oscillatory flow component (called as acoustic fields) within a fast timescale, and (iii) an additional component namely mean flow field in the slow timescale. As with most of the SAW-device-based acoustofluidic applications, operating SAW frequency is ∼1–100 MHz and displacement amplitude u_0' is ∼1–10 Å, for which acoustic Mach number $\varepsilon \ll 1$, and we can expand the flow and pressure variables asymptotically:

$$\rho = 1 + \varepsilon\rho_1 + \varepsilon^2\rho_2 + O(\varepsilon^3), \tag{9a}$$

$$p = p_0 + \varepsilon p_1 + \varepsilon^2 p_2 + O(\varepsilon^3), \tag{9b}$$

$$\mathbf{v} = \mathbf{v}_0 + \varepsilon\mathbf{v}_1 + \varepsilon^2\mathbf{v}_2 + O(\varepsilon^3). \tag{9c}$$

It is important to note here that we defined Reynolds number in such a way that it contains SAW displacement, which is of $O(\varepsilon)$ and hence, $\mathrm{Re} = O(\varepsilon)$. We define $\mathrm{Re}_s = \mathrm{Re}/\varepsilon$, which is of $O(1)$. In the present study the fast and slow timescale components are denoted as $\tilde{g}_1 = \varepsilon g_1$ and $\bar{g} = \varepsilon^2 g_2$, where g represents ρ, p, and $\mathbf{v}$.

D. Modeling of fluid hydrostatics

Substituting Eq. (9) into Eq. (4), we obtain the set of equations of $O(\varepsilon^0)$, describing the fluid hydrostatics prior to the acoustic excitations, which are expressed as

$$\frac{\partial\rho_0}{\partial t} = 0, \tag{10a}$$

$$\nabla p_0 = 0. \tag{10b}$$

We assume that the fluid is at rest before applying the acoustic excitations, i.e., $\mathbf{v}_0 = \mathbf{0}$. The solutions of the hydrostatic equations are trivial and indicate a uniform pressure and density distribution throughout the fluid.

E. Modeling of acoustic components

Equations of $O(\varepsilon^1)$ govern the acoustic fields which harmonically oscillate with the angular frequency ω, and they are given by

$$\frac{\partial\tilde{\rho}_1}{\partial t} + \nabla\cdot\tilde{\mathbf{v}}_1 = 0, \tag{11a}$$

$$\frac{\partial\tilde{\mathbf{v}}_1}{\partial t} = -\nabla\tilde{p}_1 + \frac{1}{\mathrm{Re}_s}\nabla\cdot\tilde{\tau}_1, \tag{11b}$$

where

$$\tilde{\tau}_1 = \begin{pmatrix} 2\frac{\partial\tilde{u}_1}{\partial x} & \frac{\partial\tilde{u}_1}{\partial y} + \frac{\partial\tilde{v}_1}{\partial x} \\ \frac{\partial\tilde{u}_1}{\partial y} + \frac{\partial\tilde{v}_1}{\partial x} & 2\frac{\partial\tilde{v}_1}{\partial y} \end{pmatrix} + \mathrm{De}\begin{pmatrix} \frac{\partial^2\tilde{u}_1}{\partial t\partial x} & \frac{1}{2}\left(\frac{\partial^2\tilde{u}_1}{\partial t\partial y} + \frac{\partial^2\tilde{v}_1}{\partial t\partial x}\right) \\ \frac{1}{2}\left(\frac{\partial^2\tilde{u}_1}{\partial t\partial y} + \frac{\partial^2\tilde{v}_1}{\partial t\partial x}\right) & \frac{\partial^2\tilde{v}_1}{\partial t\partial y} \end{pmatrix}.$$

The associated boundary conditions are as follows:

At the bottom

$$\tilde{u}_1 = \frac{\partial d_x}{\partial t}, \tag{12a}$$

$$\tilde{v}_1 = \frac{\partial d_y}{\partial t}. \tag{12b}$$

At side and top walls

$$\tilde{p}_1 = Z_w \mathbf{n} \cdot \tilde{\mathbf{v}}_1. \tag{13}$$

We can further simplify Eqs. (11)–(13) as the acoustic components harmonically oscillate with the same frequency as that of the actuation SAW and therefore all acoustic fields can be expressed in the form $\tilde{g}_1(x, y, t) = \widehat{g}_1(x, y)e^{it}$. Utilizing these, Eq. (11) becomes

$$i\tilde{\rho}_1 + \frac{\partial \tilde{u}_1}{\partial x} + \frac{\partial \tilde{v}_1}{\partial y} = 0, \tag{14a}$$

$$i\tilde{u}_1 = -\frac{\partial \tilde{p}_1}{\partial x} + \frac{1 + i\frac{\mathrm{De}}{2}}{\mathrm{Re}_s}\left(2\frac{\partial^2 \tilde{u}_1}{\partial x^2} + \frac{\partial^2 \tilde{u}_1}{\partial y^2} + \frac{\partial^2 \tilde{v}_1}{\partial x \partial y}\right), \tag{14b}$$

$$i\tilde{v}_1 = -\frac{\partial \tilde{p}_1}{\partial y} + \frac{1 + i\frac{\mathrm{De}}{2}}{\mathrm{Re}_s}\left(\frac{\partial^2 \tilde{u}_1}{\partial x \partial y} + \frac{\partial^2 \tilde{v}_1}{\partial x^2} + 2\frac{\partial^2 \tilde{v}_1}{\partial y^2}\right), \tag{14c}$$

and the boundary conditions at the bottom are

$$\tilde{u}_1 = id_x, \tag{15a}$$

$$\tilde{v}_1 = id_y. \tag{15b}$$

The impedance boundary at the side and top walls can further be simplified [60,62,63] and expressed as

$$\mathbf{n} \cdot \nabla \tilde{p}_1 = -\frac{i\tilde{p}_1}{Z_w}. \tag{16}$$

F. Modeling of mean flow fields

The mean flow field is governed by the second-order equations [i.e., $O(\varepsilon^2)$], which are given by

$$\frac{\partial \bar{\rho}_2}{\partial t} + \nabla \cdot \bar{\mathbf{v}}_2 + \nabla \cdot (\tilde{\rho}_1 \tilde{\mathbf{v}}_1) = 0, \tag{17a}$$

$$\frac{\partial \bar{\mathbf{v}}_2}{\partial t} + \tilde{\rho}_1 \frac{\partial \tilde{\mathbf{v}}_1}{\partial t} + (\tilde{\mathbf{v}}_1 \cdot \nabla)\tilde{\mathbf{v}}_1 = -\nabla \bar{p}_2 + \frac{1}{\mathrm{Re}_s} \nabla \cdot \bar{\tau}_2. \tag{17b}$$

In the above,

$$\bar{\tau}_2 = \begin{pmatrix} 2\frac{\partial \bar{u}_2}{\partial x} & \frac{\partial \bar{u}_2}{\partial y} + \frac{\partial \bar{v}_2}{\partial x} \\ \frac{\partial \bar{u}_2}{\partial y} + \frac{\partial \bar{v}_2}{\partial x} & 2\frac{\partial \bar{v}_2}{\partial y} \end{pmatrix} + \mathrm{De}\begin{pmatrix} \bar{s}_{xx2} & \bar{s}_{xy2} \\ \bar{s}_{yx2} & \bar{s}_{yy2} \end{pmatrix},$$

where

$$\bar{s}_{xx2} = \frac{\partial^2 \bar{u}_2}{\partial t \partial x} + \tilde{u}_1 \frac{\partial^2 \tilde{u}_1}{\partial x^2} + \tilde{v}_1 \frac{\partial^2 \tilde{u}_1}{\partial x \partial y} + (2 + b)\left(\frac{\partial \tilde{u}_1}{\partial x}\right)^2 + \left(1 + \frac{b}{4}\right)\left(\frac{\partial \tilde{v}_1}{\partial x}\right)^2 + \left(1 + \frac{b}{2}\right)\frac{\partial \tilde{u}_1}{\partial y}\frac{\partial \tilde{v}_1}{\partial x} + \frac{b}{4}\left(\frac{\partial \tilde{u}_1}{\partial y}\right)^2;$$

$$\bar{s}_{xy2} = \bar{s}_{yx2} = \frac{1}{2}\left(\frac{\partial^2 \bar{u}_2}{\partial t\,\partial y} + \frac{\partial^2 \bar{v}_2}{\partial t\,\partial x} + \tilde{u}_1\frac{\partial^2 \tilde{u}_1}{\partial x \partial y} + \tilde{u}_1\frac{\partial^2 \tilde{v}_1}{\partial x^2} + \tilde{v}_1\frac{\partial^2 \tilde{u}_1}{\partial y^2} + \tilde{v}_1\frac{\partial^2 \tilde{v}_1}{\partial x \partial y}\right)$$
$$+\left(\frac{3+b}{2}\right)\frac{\partial \tilde{u}_1}{\partial x}\frac{\partial \tilde{u}_1}{\partial y} + \left(\frac{3+b}{2}\right)\frac{\partial \tilde{v}_1}{\partial x}\frac{\partial \tilde{v}_1}{\partial y} + \left(\frac{1+b}{2}\right)\frac{\partial \tilde{u}_1}{\partial x}\frac{\partial \tilde{v}_1}{\partial x} + \left(\frac{1+b}{2}\right)\frac{\partial \tilde{v}_1}{\partial y}\frac{\partial \tilde{u}_1}{\partial y};$$
$$\bar{s}_{yy2} = \frac{\partial^2 \bar{v}_2}{\partial t\,\partial y} + \tilde{u}_1\frac{\partial^2 \tilde{v}_1}{\partial x \partial y} + \tilde{v}_1\frac{\partial^2 \tilde{v}_1}{\partial y^2} + \frac{b}{4}\left(\frac{\partial \tilde{v}_1}{\partial x}\right)^2 + \left(1+\frac{b}{4}\right)\left(\frac{\partial \tilde{u}_1}{\partial y}\right)^2$$
$$+\left(1+\frac{b}{2}\right)\frac{\partial \tilde{u}_1}{\partial y}\frac{\partial \tilde{v}_1}{\partial x} + (2+b)\left(\frac{\partial \tilde{v}_1}{\partial y}\right)^2.$$

Note here that $\bar{\boldsymbol{\tau}}_2$ can be expressed as a summation of Newtonian stress,

$$\bar{\boldsymbol{\tau}}_{2n} = \begin{pmatrix} 2\frac{\partial \bar{u}_2}{\partial x} & \frac{\partial \bar{u}_2}{\partial y} + \frac{\partial \bar{v}_2}{\partial x} \\ \frac{\partial \bar{u}_2}{\partial y} + \frac{\partial \bar{v}_2}{\partial x} & 2\frac{\partial \bar{v}_2}{\partial y} \end{pmatrix},$$

and extra stress $\bar{\boldsymbol{\tau}}_{2e} = \mathrm{De}\begin{pmatrix} \bar{s}_{xx2} & \bar{s}_{xy2} \\ \bar{s}_{yx2} & \bar{s}_{yy2} \end{pmatrix}$. To obtain the equations governing the acoustic streaming, we need to express Eq. (17) in the time-averaged form where time averaging of any flow or pressure variable, $\bar{g}(x, y, t)$, has been performed over oscillation time period $\Omega = 2\pi$ as

$$\langle \bar{g}(x, y, t)\rangle = \frac{1}{2\pi}\int_t^{t+2\pi} \bar{g}(x, y, t_1)dt_1, \tag{18}$$

where $\langle\cdot\rangle$ denotes time-averaged component. Time averaging of the product of two acoustic field components $\tilde{g}_1(x, y, t)$ and $\tilde{f}_1(x, y, t)$ can be expressed as

$$\langle \tilde{g}_1(x, y, t)\tilde{f}_1(x, y, t)\rangle = \tfrac{1}{2}\Re[\tilde{g}_1^*(x, y, 0)\tilde{f}_1(x, y, 0)], \tag{19}$$

were $\Re[\cdot]$ denotes the real component of an expression, and $\tilde{g}_1^*(.)$ indicates the complex conjugate of $\tilde{g}_1(.)$. With this time averaging, Eq. (17) can be expressed at steady state as

$$\nabla\cdot\langle\bar{\mathbf{v}}_2\rangle + \nabla\cdot\langle\tilde{\rho}_1\tilde{\mathbf{v}}_1\rangle = 0, \tag{20a}$$
$$\nabla\cdot\left(\frac{1}{\mathrm{Re}_s}\langle\bar{\tau}_2\rangle - \langle\tilde{\mathbf{v}}_1\tilde{\mathbf{v}}_1\rangle - \langle\bar{p}_2\rangle\mathbf{I}\right) = 0. \tag{20b}$$

The associated boundary conditions are described below. At the bottom, the conservation of mass flux provides us the required boundary condition, whereas for the sides and top walls, zero velocity is prescribed:

$$\text{At bottom}: \langle\bar{\mathbf{v}}_2\rangle = -\langle\tilde{\rho}_1\tilde{\mathbf{v}}_1\rangle, \tag{21a}$$
$$\text{At sides and top}: \langle\bar{\mathbf{v}}_2\rangle = 0. \tag{21b}$$

III. RESULTS AND DISCUSSION

A. Choices of parameters

The governing equations (14) and (20), along with the boundary conditions prescribed by Eqs. (15), (16), and (21), are solved for $0.08 \leqslant \mathrm{Re} \leqslant 0.32$. This range of Re is chosen since the density ρ_0 for second-order fluid is $\sim$1000 kg m^{-3}, sonic speed c_0 is $\sim$1000 m/s, viscosity η is $\sim 10^{-4} - 10^{-3}$ Pa s. SAW displacement amplitude $u'_0 \sim 0.1{-}1$ Å, and the operating SAW frequency is $\sim$1–100 MHz. Along with that Reynolds number range, Deborah number is taken as $0 \leqslant \mathrm{De} \leqslant 1$, b is taken within $0 \leqslant b \leqslant 100$, and the acoustic impedance of the wall material and the attenuation coefficient of the SAW are taken as $Z_w = 0.743$ and $c_d = 4.741 \times 10^{-3}$, respectively. ξ, ε, and k_x are taken as 0.86, 1×10^{-5}, and 0.374 74, respectively. With these parameters, we studied

the influence of Re, De, and b on the acoustic fields and the acoustic streaming. The acoustophoretic particle motions are also predicted by accounting for the drag forces and the acoustic radiation forces acting on the particles.

B. Mesh convergence analysis

Before presenting the results, a mesh convergence analysis has been performed to confirm the fact that the spatial resolution considered for the numerical study is adequate to capture the underlying physics. As evident from previous related studies [53,60,64], we need a very fine mesh near the boundary. The thickness of the boundary layer can be estimated in dimensional form as $\delta' = \sqrt{2\eta/\rho_0\omega}$, and in dimensionless form, it is given by $\delta = \delta'/k^{-1}$. We have defined region of thickness 10δ near each boundary and prescribed very fine mesh within that (see Figs. S1(a) and S1(b) in the Supplemental Material [65]). The rest of the computational domain has a relatively large mesh size (called bulk mesh size), d_{bulk}. We have taken $d_{\text{bulk}} = 10\delta$ and progressively refined the boundary mesh size, d_b. We define a relative convergence function $C(g)$ for solution g relative to its reference solution g_{ref} following similar previous studies [60,64]:

$$C(g) = \sqrt{\frac{\int (g - g_{\text{ref}})^2 dxdy}{\int (g_{\text{ref}})^2 dxdy}}. \tag{22}$$

Here g_{ref} is obtained for $d_b = 0.2\delta$, and we have plotted the mesh convergence study results in Fig. S1(c) (see Supplemental Material [65]) for various δ/d_b ranging from 1 to 4.4. Based on our study we found $\delta/d_b = 3$ is suitable for all convergence function to be bellow 10^{-2}, and we have chosen this value for all the simulations presented in the work. Please note that any further refinement in the bulk mesh size (i.e., d_{bulk}) does not affect the simulation results. With these simulation settings we first validated our model with the existing literature (see Fig. S2 in the Supplemental Material [65]), and after successful validation we present the acoustic fields, acoustic streaming, and the acoustophoretic particle motions in the following sections.

C. Acoustic fields

Figure 2 shows the acoustic pressure and velocity fields in a microchannel of width $W = 2\pi/k_x$ and height $H = \pi/2k_x$ excited by a standing SAW at $t = 2\pi n$, where n is an integer. The acoustic pressure $\widehat{p}_1$, varies between 2.17×10^{-5} (red) and -2.17×10^{-5} (blue), whereas acoustic velocity magnitude $|\widehat{\mathbf{v}}_1|$ varies within zero (blue) and 1.76×10^{-5} (red). It is evident from Eq. (14) that the acoustic field does not depend on the material constant ratio, b. In addition to that, Re and De have a negligible impact on the acoustic pressure and velocity profiles. For instance, the maximum acoustic pressure $\widehat{p}_{1\,\max} = 2.1687 \times 10^{-5}$ at $\text{Re} = 0.08$ and $\text{De} = 0$, whereas at $\text{Re} = 0.32$ and $\text{De} = 1$, $\widehat{p}_{1\,\max} = 2.1720 \times 10^{-5}$, indicating less than 0.15% variation over a wide range of Reynolds number ($0.08 \leqslant \text{Re} \leqslant 0.32$) and Deborah number $0 \leqslant \text{De} \leqslant 1$. This is a remarkable result, and it implies that the acoustic fields hardly depend on the fluid inertia or the viscous effects. It is clear that the acoustic pressure and velocity are oscillating with time (see Supporting Material video [65]), and the maximum acoustic pressure $\tilde{p}_{1\,\max}$ is observed to be 2.30×10^{-5}, whereas the maximum acoustic velocity magnitude ($|\mathbf{v}_1|_{\max}$) is estimated to be 2.20×10^{-5}, which is much higher than the maximum acoustic velocity associated with the SSAW, i.e., $\varepsilon = 1 \times 10^{-5}$. This ensures that there are reflections of the acoustic waves on the microchannel walls which are attributed to the impedance mismatch between the wall material ($Z_w = 0.743$) and fluid (dimensionless impedance of the fluid is 1).

D. Acoustic streaming

Figure 3(a) shows the acoustic streaming velocity field $|\langle\bar{\mathbf{v}}_2\rangle|$ inside the microchannel of width $W = 2\pi/k_x$ and height $H = \pi/2k_x$. We observe four streaming vortices similar to that for

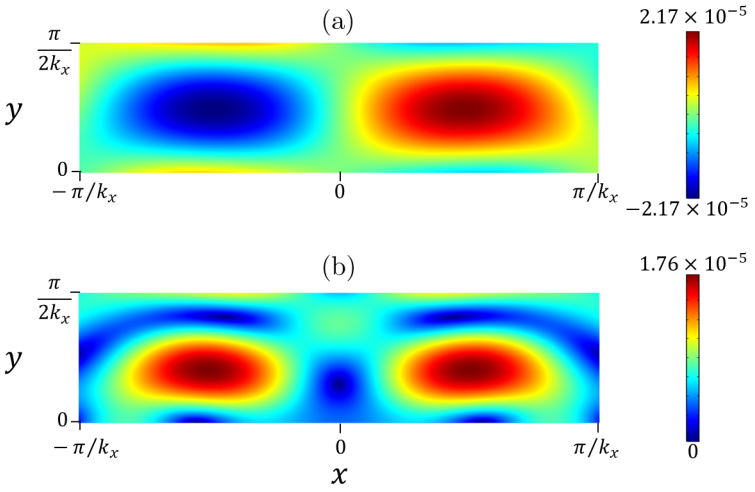

FIG. 2. (a) Color plot of acoustic pressure $\widehat{p}_1$ and (b) velocity magnitude $|\widehat{\mathbf{v}}_1|$ at $t = 2\pi n$ for a microchannel of width $W = 2\pi/k_x$ and height $H = \pi/2k_x$ excited by a standing SAW specified by Eq. (7). The plot represents pressure and velocity magnitude for $0.08 \leqslant \mathrm{Re} \leqslant 0.32$ and $0 \leqslant \mathrm{De} \leqslant 1$. These values show negligible variation (<0.15%) over these ranges. The acoustic impedance of the microchannel wall material, the attenuation coefficient of the SAW, and the acoustic Mach number are taken as $Z_w = 0.743$, $c_d = 4.741 \times 10^{-3}$, and $\varepsilon = 1 \times 10^{-5}$, respectively. The SAW amplitude ratio (ξ) and SAW wave vector (k_x) are taken as 0.86 and 0.374 74, respectively.

Newtonian fluids (i.e., $\mathrm{De} = 0$). A large acoustic streaming velocity magnitude is observed near the bottom boundary, and there exists a sharp velocity gradient adjacent to it. Figure 3(b) illustrates this sharp velocity gradient and the variation of $|\langle\bar{\mathbf{v}}_2\rangle|$ along the channel height at $x = \pm\frac{1}{8}H$ and $x = \pm\frac{3}{8}H$. The maximum acoustic streaming velocity, $|\langle\bar{\mathbf{v}}_2\rangle|_{\max}$, is located near the bottom boundary at $x = \pm\frac{1}{8}H$, whereas at $x = \pm\frac{3}{8}H$ the acoustic streaming is slightly suppressed due to the interaction with adjacent sidewalls. We notice that the color plot of the acoustic streaming velocity distribution remains the same for all Reynolds numbers and Deborah numbers except the maximum acoustic streaming velocity magnitude $|\langle\bar{\mathbf{v}}_2\rangle|_{\max}$ varies.

Figure 4 illustrates the variation of $|\langle\bar{\mathbf{v}}_2\rangle|_{\max}$ as a function of De for $b = 0$, 50, and 100 at $\mathrm{Re} = 0.08$, 0.16, 0.24, and 0.32. It can be concluded that with increasing Reynolds number, the acoustic streaming velocity is enhanced. This is attributed to the fact that with increasing Reynolds number, either the inertial force increases or the viscous force decreases, leading to an overall increase in the driving force for acoustic streaming. However, we found that the acoustic streaming velocity is first enhanced with an increase in Deborah number, and thereafter, a further increase in Deborah number causes suppression of the acoustic streaming. This is counterintuitive and requires further explanation. We dig into the characterizations of the driving forces and how they are influenced by the extra stress components associated with the second-order fluids. It is observed that even though the variation of acoustic fields over Deborah number is extremely small, the dependence of the time-averaged momentum-flux-density tensor, i.e., $\langle\tilde{\mathbf{v}}_1\tilde{\mathbf{v}}_1\rangle$ on Deborah number cannot be neglected. Importantly, with increasing Deborah number, the time-averaged momentum-flux-density tensor increases, which helps in enhancing the acoustic streaming, whereas the extra stress components suppress the acoustic streaming. Due to this complex interplay, there exists a cutoff Deborah number ($\mathrm{De}_{\mathrm{cutoff}}$) below which larger acoustic streaming as compared to that of a Newtonian fluid is encountered. In Fig. 4, the acoustic streaming enhanced zone has been shown in cyan color, and for $\mathrm{Re} = 0.08$ and $b = 0$, the cutoff value is $\mathrm{De}_{\mathrm{cutoff}} = 0.44$, and above that Deborah number, the acoustic streaming is suppressed more and more with increasing Deborah number [see

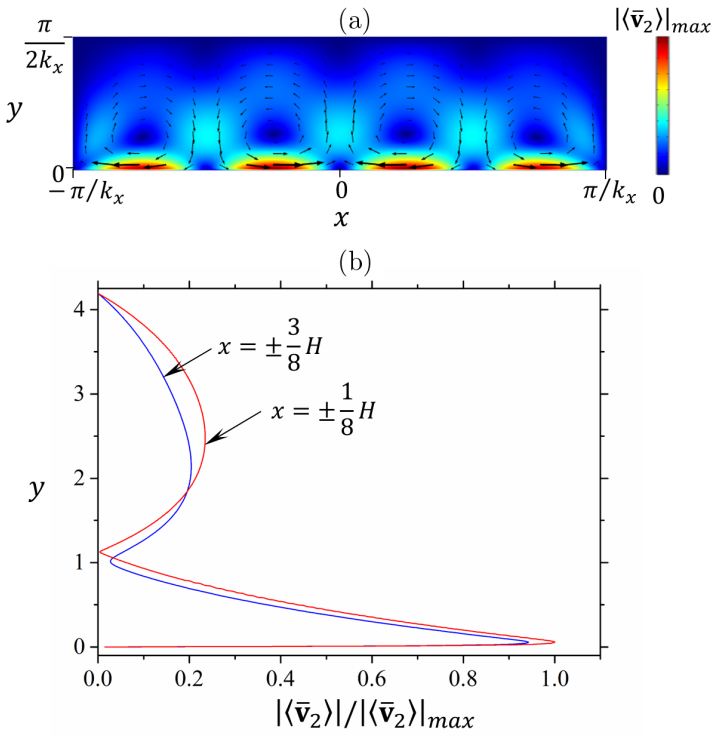

FIG. 3. (a) Acoustic streaming velocity field (color plot) and associated vector plot (black arrows) for the standing SAW driven microchannel of width $W = 2\pi/k_x$ and height $H = \pi/2k_x$ filled with second-order fluid where $|\langle\bar{\mathbf{v}}_2\rangle|_{\max}$ denotes the maximum acoustic streaming velocity magnitude. The plots show generic acoustic streaming velocity field for $0.08 \leqslant \mathrm{Re} \leqslant 0.32$, $0 \leqslant \mathrm{De} \leqslant 1$, and $0 \leqslant b \leqslant 1$. The acoustic impedance of the microchannel wall material, the attenuation coefficient of the SAW, and the acoustic Mach number are taken as $Z_w = 0.743$, $c_d = 4.741 \times 10^{-3}$, and $\varepsilon = 1 \times 10^{-5}$, respectively. The SAW amplitude ratio (ξ) and SAW wave vector (k_x) are taken as 0.86 and 0.374 74, respectively. (b) Variation of rescaled acoustic streaming velocity magnitude, i.e., $|\langle\bar{\mathbf{v}}_2\rangle|/|\langle\bar{\mathbf{v}}_2\rangle|_{\max}$, along y at $x = \pm\frac{3}{8}H$ (blue) and $x = \pm\frac{1}{8}H$ (red).

Fig. 4(a)]. An increase in the material constant ratio, b, effectively implicates an increase in the viscous force, which causes further suppression of the acoustic streaming, leading to a lower $\mathrm{De}_{\mathrm{cutoff}}$ value. For instance, at $\mathrm{Re} = 0.08$ and $b = 50$, the acoustic streaming enhanced zone is restricted to $0 < \mathrm{De} < 0.16$, whereas for $\mathrm{Re} = 0.08$, $b = 100$, there is no enhancement of the acoustic streaming at all. This is a very important result that provides us with the flexibility to control and manipulate acoustic streaming by regulating the fluid rheology without affecting the acoustic fields. Our present study also reveals that a stronger acoustic streaming is manifested at higher Reynolds number, which ensures a wider range of Deborah number for acoustic streaming enhancement for higher b values ($b = 50$, and/or 100) with exceptions at low values of b, where slightly lower $\mathrm{De}_{\mathrm{cutoff}}$ is observed.

E. Acoustophoretic motion of the microparticles

One of the primary uses of acoustofluidic devices is the manipulation of micron-size cells or particles, as these objects experience acoustic radiation force due to the scattering of the acoustic waves onto them. This acoustophoretic motion of the particles can be predicted for a steady acoustic streaming field, and in this section, we consider spherical particles of radius a', density ρ_p', and compressibility κ_p' suspended in the second-order fluids. We made these dimensionless as $a = a'/k^{-1}$, $\rho_p = \rho_p'/\rho_0$, and $\kappa_p = \kappa_p'/\kappa_0$, where κ_0 is the compressibility of the fluid. The particle

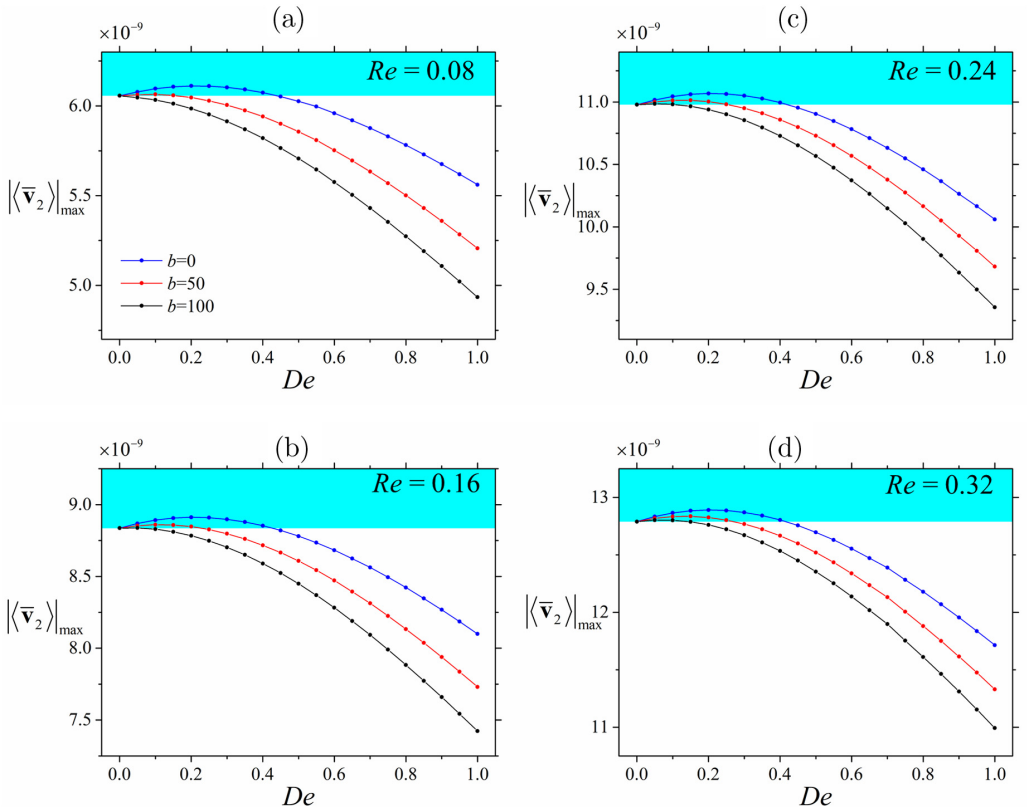

FIG. 4. Dependence of $|\langle\bar{\mathbf{v}}_2\rangle|_{\max}$ on De for $b = 0$ (blue), 50 (red), and 100 (black) at (a) Re $= 0.08$, (b) Re $= 0.16$, (c) Re $= 0.24$, and (d) Re $= 0.32$ for standing SAW driven microchannel of width $W = 2\pi/k_x$ and height $H = \pi/2k_x$ filled with second-order fluid. The acoustic impedance of the microchannel wall material, the attenuation coefficient of the SAW, and the acoustic Mach number are taken as $Z_w = 0.743$, $c_d = 4.741 \times 10^{-3}$, and $\varepsilon = 1 \times 10^{-5}$, respectively. The SAW amplitude ratio (ξ) and SAW wave vector (k_x) are taken as 0.86 and 0.37474, respectively. The cyan region indicates the enhanced acoustic streaming zone.

suspension is diluted enough so that the interparticle interactions can be neglected. For small particle size, i.e., ($a \ll 2\pi$), the acoustic radiation force acting on the particle can therefore be described in dimensionless form as [21]

$$\mathbf{F}^{\text{rad}} = -\nabla U \quad \text{where} \quad U = 2\pi a^3\left(\tfrac{1}{3}\langle\tilde{p}_1\tilde{p}_1\rangle f_0 - \tfrac{1}{2}\langle|\tilde{\mathbf{v}}_1|^2\rangle f_1\right), \tag{23}$$

where monopole and dipole scattering coefficients are given by $f_0 = 1 - \kappa_p$ and $f_1 = \frac{2(\rho_p - 1)}{2\rho_p + 1}$, respectively. The drag force acting on the particle is estimated via Stokes formula $\mathbf{F}^{\text{drag}} = \frac{6\pi a\varepsilon}{\text{Re}}(\langle\bar{\mathbf{v}}_2\rangle - \bar{\mathbf{v}}_p)$, and the motion of the microparticles can be predicted via Newton's second law: $\frac{4}{3}\pi a_p^3\rho_p\frac{d\bar{\mathbf{v}}_p}{dt} = \mathbf{F}^{\text{rad}} + \mathbf{F}^{\text{drag}}$. At steady state, the particle velocity field is obtained as $\bar{\mathbf{v}}_{p,s} = \langle\bar{\mathbf{v}}_2\rangle + \frac{\text{Re}}{6\pi a\varepsilon}\mathbf{F}^{\text{rad}}$, which indicates that the acoustophoretic particle velocity is increased by the acoustic radiation force.

Figures 5 and 6 show the acoustophoretic particle trajectories at Re $= 0.08$ for particles of various sizes over the Deborah number and b ranging from 0 to 1 and 0 to 100, respectively. For $a = 0.05$, the particles closely follow the acoustic streaming velocity vector (Fig. 5), whereas for $a = 0.5$ the particle trajectory shows resemblance to the acoustic radiation force vectors [Fig. 6(a)]. This indicates that for small particles (i.e., $a = 0.05$), the acoustic radiation force is very little and

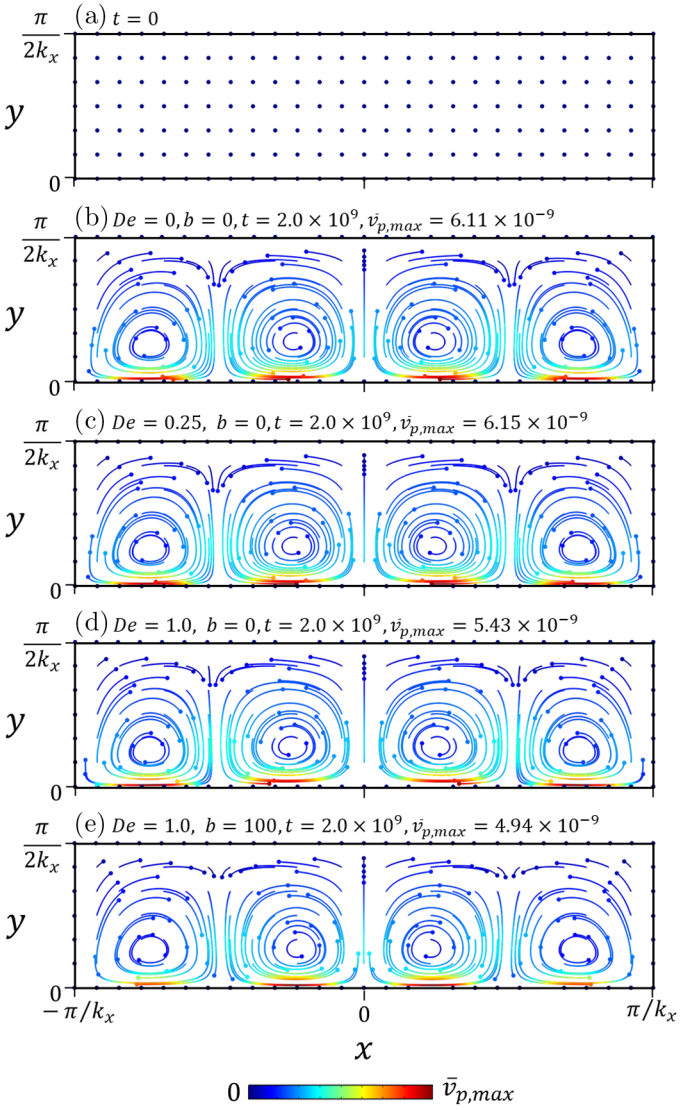

FIG. 5. (a) Initial positions of the particles and (b)–(e) their trajectories in a standing SAW driven microchannel of width $W = 2\pi/k_x$ and height $H = \pi/2k_x$ filled with second-order fluid. Trajectories are shown for particle size $a = 0.05$ at (b) De $= 0$, $b = 0$; (c) De $= 0.25$, $b = 0$; (d) De $= 1.0$, $b = 0$; and (e) De $= 1.0$, $b = 100$. The trajectories are shown for particle density $\rho_p = 1.05$ and particle compressibility $\kappa_p = 0.56$ at Re $= 0.08$. The color associated with the particle trajectories indicates the particle velocities as shown in the color bar, where red and blue show maximum ($\bar{v}_{p,\max}$) and zero particle velocities, respectively.

the particle motion is governed by the viscous drag of the fluid [Figs. 5(b)–5(e)]. With the initial particle configuration shown in Fig. 5(a), the maximum particle velocity for $a = 0.05$ at De $= 0$ and $b = 0$ [see Fig. 5(b)] is observed as $\bar{v}_{p,\max} = 6.11 \times 10^{-9}$, which is slightly higher than the corresponding maximum acoustic streaming velocity $|\langle\bar{\mathbf{v}}_2\rangle|_{\max} = 6.06 \times 10^{-9}$. For De $= 0.25$, the acoustic streaming velocity $|\langle\bar{\mathbf{v}}_2\rangle|_{\max}$ increases to 6.11×10^{-9} and the maximum estimated particle velocity is 6.15×10^{-9} [Fig. 5(c)]. As De and b increase further, the particle motion slows down due to suppression of the acoustic streaming [Fig. 5(d)]. With increasing particle size, the acoustic

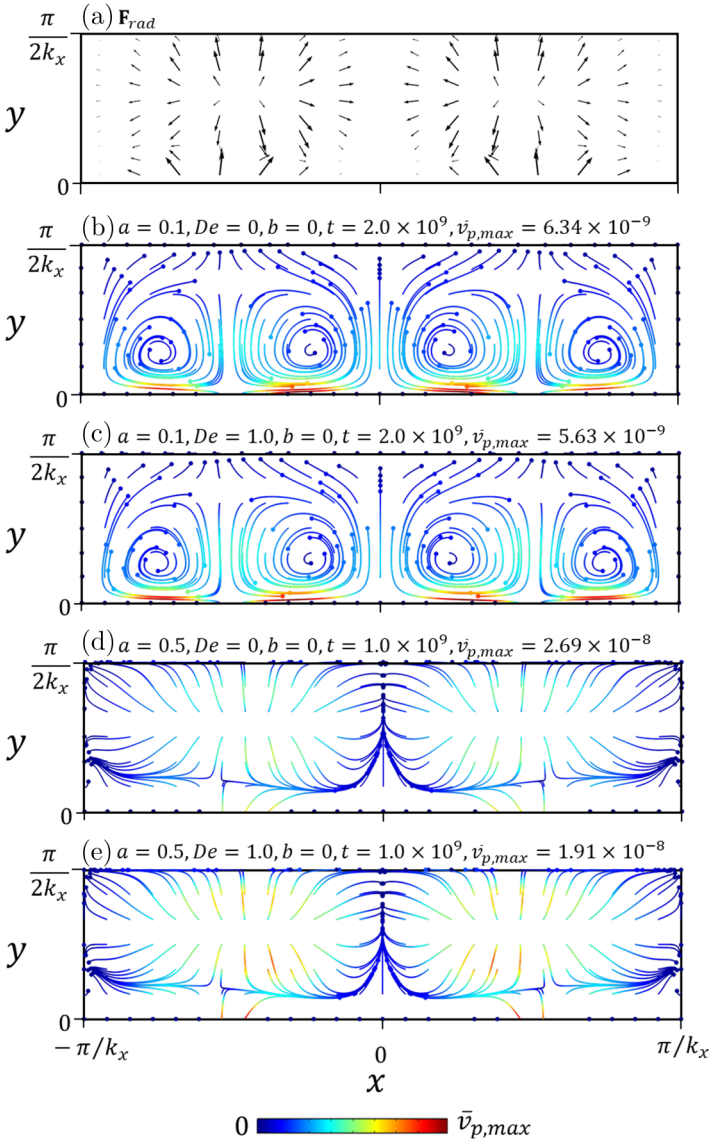

FIG. 6. (a) Vector plot of acoustic radiation force. (b)–(e) Particle trajectories in a standing SAW driven microchannel of width $W = 2\pi/k_x$ and height $H = \pi/2k_x$ filled with second-order fluid with initial particle configuration as shown in Fig. 5(a). Trajectories are shown for (b) $a = 0.1$, De $= 0$, $b = 0$; (c) $a = 0.1$, De $= 1.0$, $b = 0$; (d) $a = 0.5$, De $= 0$, $b = 0$; and (e) $a = 0.5$, De $= 1.0$, $b = 0$. The trajectories are shown for particle density $\rho_p = 1.05$ and particle compressibility $\kappa_p = 0.56$ at Re $= 0.08$. The color bar is associated with the particle trajectories (b)–(e), and the color indicates the particle velocities where red and blue show maximum ($\bar{v}_{p,\max}$) and zero particle velocities, respectively.

radiation force increases faster than the viscous drag, and for large particle size (i.e., $a = 0.5$), the particle trajectory is maneuvered by the acoustic radiation force [Figs. 6(c)–6(d)]. At intermediate particle size such as $a = 0.1$, both acoustic radiation force and the viscous force are prominent, and the particle trajectory follows a path governed by the superposition of both these forces [Figs. 6(a) and 6(b)]. Interestingly, the particle trajectories are not much influenced by the variation of Re, De, and b values (see Figs. S3 and S4 in the Supplemental Material [65] for microparticle trajectories at

Re = 0.20 and 0.32), which confirms that the variation of second-order fluid properties can suppress or enhance the acoustic streaming without altering the acoustic radiation force significantly.

IV. CONCLUSION

In this article we have presented a multiple-timescales-based model and carried out a numerical study to characterize the acoustic streaming in a bottom-actuated microchannel filled with second-order fluids. The governing Navier-Stokes equations are expressed in dimensionless form, and the perturbation technique is used to separate the slow and fast timescales associated with the acoustofluidic system. The acoustic fields and the acoustic streaming velocities are estimated for a wide range of Reynolds number Re and Deborah number De, and the material constant ratio b. With increasing Re, the increasing inertia or decreasing viscous effect essentially increase acoustic streaming. Our study reveals that for relatively low De, the second-order fluid rheology can enhance the acoustic streaming values, and beyond a cutoff value (De_{cutoff}), increasing De gradually suppresses the acoustic streaming due to the extra stresses present in the fluids. This cutoff value strongly depends on Re and b. The microparticle trajectories are influenced by the particle size, and based on the size, either drag force or acoustic radiation force or both control the paths of the particle motion. However, they are negligibly influenced by Re, De, and b. This study is extremely important in the context of acoustofluidic particle sorting and manipulation, as it provides us the flexibility to enhance or suppress acoustic streaming by altering fluid rheology without significantly affecting the acoustic radiation forces.

ACKNOWLEDGMENTS

This work was funded by National Science Foundation Grant No. CMI-2108795, which is gratefully acknowledged. Pradipta Kr. Das gratefully acknowledges a University of South Florida Presidential Fellowship.

[1] M. Faraday, XVII. On a peculiar class of acoustical figures, And on certain forms assumed by groups of particles upon vibrating elastic surfaces, Philos. Trans. R. Soc. London **121**m 299 (1831).
[2] H. Schlichting, Über die stabilität der couetteströmung, Ann. Phys. **406**, 905 (1932).
[3] L. Rayleigh, On waves propagated along the plane surface of an elastic solid, Proc. London Math. Soc. **1**, 4 (1885).
[4] C. Eckart, Vortices and streams caused by sound waves, Phys. Rev. **73**, 68 (1948).
[5] W. L. Nyborg, Acoustic streaming near a boundary, J. Acoust. Soc. Am. **30**, 329 (1958).
[6] C. P. Lee and T. G. Wang, Near-boundary streaming around a small sphere due to two orthogonal standing waves, J. Acoust. Soc. Am. **85**, 1081 (1989).
[7] M. F. Hamilton, Y. A. Ilinskii, and E. A. Zabolotskaya, Acoustic streaming generated by standing waves in two-dimensional channels of arbitrary width, J. Acoust. Soc. Am. **113**, 153 (2003).
[8] J. Holtsmark, I. Johnsen, T. Sikkeland, and S. Skavlem, Boundary layer flow near a cylindrical obstacle in an oscillating incompressible fluid, J. Acoust. Soc. Am. **26**, 102 (1954).
[9] S. J. Lighthill, Acoustic streaming, J. Sound Vib. **61**, 391 (1978).
[10] Y. Huang, P. K. Das, and V. R. Bhethanabotla, Surface acoustic waves in biosensing applications, Sens. Actuators Rep. **3**, 100041 (2021).
[11] T. Frommelt, M. Kostur, M. Wenzel-Schäfer, P. Talkner, P. Hänggi, and A. Wixforth, Microfluidic Mixing via Acoustically Driven Chaotic Advection, Phys. Rev. Lett. **100**, 034502 (2008).
[12] A. R. Rezk, A. Qi, J. R. Friend, W. H. Li, and L. Y. Yeo, Uniform mixing in paper-based microfluidic systems using surface acoustic waves, Lab Chip **12**, 773 (2012).
[13] R. Shilton, M. K. Tan, L. Y. Yeo, and J. R. Friend, Particle concentration and mixing in microdrops driven by focused surface acoustic waves, J. Appl. Phys. **104**, 014910 (2008).

[14] W.-K. Tseng, J.-L. Lin, W.-C. Sung, S.-H. Chen, and G.-B. Lee, Active micro-mixers using surface acoustic waves on Y-cut 128° LiNbO3, J. Micromech. Microeng. **16**, 539 (2006).
[15] J. Liu, S. Li, and V. R. Bhethanabotla, Integrating metal-enhanced fluorescence and surface acoustic waves for sensitive and rapid quantification of cancer biomarkers from real matrices, ACS Sensors **3**, 222 (2018).
[16] B. J. Davidson, Heat transfer from a vibrating circular cylinder, Int. J. Heat Mass Transfer **16**, 1703 (1973).
[17] A. Gopinath and A. F. Mills, Convective heat transfer from a sphere due to acoustic streaming, J. Acoust. Soc. Am. **94**, 1773 (1993).
[18] M. Legay, N. Gondrexon, S. Le Person, P. Boldo, and A. Bontemps, Enhancement of heat transfer by ultrasound: Review and recent advances, Int. J. Chem. Eng. **2011**, 670108 (2011).
[19] J. G. Kaufmann, M. P. Y. Desmulliez, Y. Tian, D. Price, M. Hughes, N. Strusevich, C. Bailey, C. Liu, and D. Hutt, Megasonic agitation for enhanced electrodeposition of copper, Microsyst. Technol. **15**, 1245 (2009).
[20] J. S. Bach and H. Bruus, Theory of pressure acoustics with viscous boundary layers and streaming in curved elastic cavities, J. Acoust. Soc. Am. **144**, 766 (2018).
[21] L. P. Gor'kov, On the forces acting on a small particle in an acoustical field in an ideal fluid, Sov. Phys. Dokl. **6**, 773 (1962).
[22] J. T. Karlsen and H. Bruus, Forces acting on a small particle in an acoustical field in a thermoviscous fluid, Phys. Rev. E **92**, 043010 (2015).
[23] F. Guo *et al.*, Three-dimensional manipulation of single cells using surface acoustic waves, Proc. Natl. Acad. Sci. **113**, 1522 (2016).
[24] A. Ozcelik, J. Rufo, F. Guo, Y. Gu, P. Li, J. Lata, and T. J. Huang, Acoustic tweezers for the life sciences, Nat. Methods **15**, 1021 (2018).
[25] A. Sano, Y. Matsui, and S. Shiokawa, New manipulator based on surface acoustic wave streaming, Japan. J. Appl. Phys. **37**, 2979 (1998).
[26] G. Celik Cogal, P. K. Das, S. Li, A. Uygun Oksuz, and V. R. Bhethanabotla, Unraveling the autonomous motion of polymer-based catalytic micromotors under chemical−acoustic hybrid power, Adv. NanoBiomed. Research **1**, 2000009 (2021).
[27] S. Cular, D. W. Branch, V. R. Bhethanabotla, G. D. Meyer, and H. G. Craighead, Removal of nonspecifically bound proteins on microarrays using surface acoustic waves, IEEE Sensors J. **8**, 314 (2008).
[28] S. K. R. S. Sankaranarayanan, S. Cular, V. R. Bhethanabotla, and B. Joseph, Flow induced by acoustic streaming on surface-acoustic-wave devices and its application in biofouling removal: A computational study and comparisons to experiment, Phys. Rev. E **77**, 066308 (2008).
[29] M. Richardson, P. K. Das, S. Morrill, K. J. Suthar, S. K. R. S. Sankaranarayanan, and V. R. Bhethanabotla, Removal of non-specifically bound proteins using Rayleigh waves generated on ST-quartz substrates, Sensors **22** (2022).
[30] B. Hammarström, N. R. Skov, K. Olofsson, H. Bruus, and M. Wiklund, Acoustic trapping based on surface displacement of resonance modes, J. Acoust. Soc. Am. **149**, 1445 (2021).
[31] J. Lee, S.-Y. Teh, A. Lee, H. H. Kim, C. Lee, and K. K. Shung, Single beam acoustic trapping, Appl. Phys. Lett. **95**, 073701 (2009).
[32] M. Evander and J. Nilsson, Acoustofluidics 20: Applications in acoustic trapping, Lab Chip **12**, 4667 (2012).
[33] S. C. Takatori, R. De Dier, J. Vermant, and J. F. Brady, Acoustic trapping of active matter, Nat. Commun. **7**, 10694 (2016).
[34] G. Celik Cogal, P. K. Das, G. Yurdabak Karaca, V. R. Bhethanabotla, and A. Uygun Oksuz, Fluorescence detection of miRNA-21 using Au/Pt bimetallic tubular micromotors driven by chemical and surface acoustic wave forces, ACS Appl. Bio Mater. (2021).
[35] T. J. Lyford, P. J. Millard, and M. P. d. Cunha, in *2012 IEEE International Ultrasonics Symposium* (IEEE, New York, 2012), p. 1216.
[36] D. Taller, K. Richards, Z. Slouka, S. Senapati, R. Hill, D. B. Go, and H.-C. Chang, On-chip surface acoustic wave lysis and ion-exchange nanomembrane detection of exosomal RNA for pancreatic cancer study and diagnosis, Lab Chip **15**, 1656 (2015).

[37] D. J. Collins, T. Alan, and A. Neild, Particle separation using virtual deterministic lateral displacement (vDLD), Lab Chip **14**, 1595 (2014).
[38] D. J. Collins, A. Neild, and Y. Ai, Highly focused high-frequency travelling surface acoustic waves (SAW) for rapid single-particle sorting, Lab Chip **16**, 471 (2016).
[39] T. Franke, S. Braunmüller, L. Schmid, A. Wixforth, and D. A. Weitz, Surface acoustic wave actuated cell sorting (SAWACS), Lab Chip **10**, 789 (2010).
[40] P. Li *et al.*, Acoustic separation of circulating tumor cells, Proc. Natl. Acad. Sci. **112**, 4970 (2015).
[41] O. Jakobsson, C. Grenvall, M. Nordin, M. Evander, and T. Laurell, Acoustic actuated fluorescence activated sorting of microparticles, Lab Chip **14**, 1943 (2014).
[42] J. Friend and L. Y. Yeo, Microscale acoustofluidics: Microfluidics driven via acoustics and ultrasonics, Rev. Mod. Phys. **83**, 647 (2011).
[43] J. Rufo, F. Cai, J. Friend, M. Wiklund, and T. J. Huang, Acoustofluidics for biomedical applications, Nat. Rev. Methods Primers **2**, 30 (2022).
[44] K. Yasuda and T. Kamakura, Acoustic radiation force on micrometer-size particles, Appl. Phys. Lett. **71**, 1771 (1997).
[45] H. Bruus, Acoustofluidics 7: The acoustic radiation force on small particles, Lab Chip **12**, 1014 (2012).
[46] G. R. Torr, The acoustic radiation force, Am. J. Phys. **52**, 402 (1984).
[47] J. Nam, H. Lim, D. Kim, and S. Shin, Separation of platelets from whole blood using standing surface acoustic waves in a microchannel, Lab Chip **11**, 3361 (2011).
[48] M. Wu *et al.*, Circulating tumor cell phenotyping via high-throughput acoustic separation, Small **16**, 2004438 (2020).
[49] T. Baasch, A. Pavlic, and J. Dual, Acoustic radiation force acting on a heavy particle in a standing wave can be dominated by the acoustic microstreaming, Phys. Rev. E **100**, 061102(R) (2019).
[50] L. Ren, D. Zhou, Z. Mao, P. Xu, T. J. Huang, and T. E. Mallouk, Rheotaxis of bimetallic micromotors driven by chemical–acoustic hybrid power, ACS Nano **11**, 10591 (2017).
[51] J. G. S. Moo, C. C. Mayorga-Martinez, H. Wang, W. Z. Teo, B. H. Tan, T. D. Luong, S. R. Gonzalez-Avila, C.-D. Ohl, and M. Pumera, Bjerknes forces in motion: Long-range translational motion and chiral directionality switching in bubble-propelled micromotors via an ultrasonic pathway, Adv. Funct. Mater. **28**, 1702618 (2018).
[52] M. Hoyos and A. Castro, Controlling the acoustic streaming by pulsed ultrasounds, Ultrasonics **53**, 70 (2013).
[53] P. B. Muller and H. Bruus, Theoretical study of time-dependent, ultrasound-induced acoustic streaming in microchannels, Phys. Rev. E **92**, 063018 (2015).
[54] J. S. Bach and H. Bruus, Suppression of Acoustic Streaming in Shape-Optimized Channels, Phys. Rev. Lett. **124**, 214501 (2020).
[55] K. R. Frater, Acoustic streaming in an elastico-viscous fluid, J. Fluid Mech. **30**, 689 (1967).
[56] R. L. Powell, Acoustic streaming reversal by a finite amplitude sound wave in a non-Newtonian fluid, J. Acoust. Soc. Am. **71**, S31 (1982).
[57] A. A. Doinikov, J. Fankhauser, and J. Dual, Nonlinear dynamics of a solid particle in an acoustically excited viscoelastic fluid. I. Acoustic streaming, Phys. Rev. E **104**, 065107 (2021).
[58] A. A. Doinikov, J. Fankhauser, and J. Dual, Nonlinear dynamics of a solid particle in an acoustically excited viscoelastic fluid. II. Acoustic radiation force, Phys. Rev. E **104**, 065108 (2021).
[59] P. K. Das, A. D. Snider, and V. R. Bhethanabotla, Acoustic streaming in second-order fluids, Phys. Fluids **32**, 123103 (2020).
[60] N. Nama, R. Barnkob, Z. Mao, C. J. Kähler, F. Costanzo, and T. J. Huang, Numerical study of acoustophoretic motion of particles in a PDMS microchannel driven by surface acoustic waves, Lab Chip **15**, 2700 (2015).
[61] C. Devendran, T. Albrecht, J. Brenker, T. Alan, and A. Neild, The importance of travelling wave components in standing surface acoustic wave (SSAW) systems, Lab Chip **16**, 3756 (2016).
[62] P. K. Das, A. D. Snider, and V. R. Bhethanabotla, Acoustothermal heating in surface acoustic wave driven microchannel flow, Phys. Fluids **31**, 106106 (2019).

[63] H. Bruus, Acoustofluidics 2: Perturbation theory and ultrasound resonance modes, Lab Chip **12**, 20 (2012).

[64] P. B. Muller, R. Barnkob, M. J. H. Jensen, and H. Bruus, A numerical study of microparticle acoustophoresis driven by acoustic radiation forces and streaming-induced drag forces, Lab Chip **12**, 4617 (2012).

[65] See Supplemental Material at http://link.aps.org/supplemental/10.1103/PhysRevFluids.7.074404 for mesh convergence, code validation, and microparticle trajectories at $\mathrm{Re} = 0.20$ and 0.32.